I&EC research
Industrial & Engineering Chemistry Research

pubs.acs.org/IECR

Article

Microporous Graphite Composites of Tailorable Porosity, Surface Wettability, and Water Permeability for Fuel Cell Bipolar Plates

Aswin Prathap Pitchiya, Ngoc-Tram Le, Zackary A. Putnam, Michael Harrington, and Sitaraman Krishnan*

Cite This: https://doi.org/10.1021/acs.iecr.1c01737

Read Online

ACCESS | Metrics & More | Article Recommendations | Supporting Information

ABSTRACT: To address the water management problem in proton-exchange membrane fuel cells, porous graphite composites were prepared by incorporating sacrificial pore-forming agents in the blend of graphite and a phenolic resin formed into a flat plate using compression molding. Sucrose was found to be an effective porogen in the porous plate production process. The effects of relative amounts of graphite, polymer, and porogen in the composite were studied. Bipolar plate properties such as the water uptake by wicking and vacuum infusion, gas-breakthrough pressure across the water-infused pores, electrical conductivity, and flexural strength of the plates were measured and correlated with the plate composition. The plate porosity was evaluated by determining the masses of dry and water-infused plates in air and under water. The porosity, ε, showed a linear increase with an increase in the porogen concentration in the range of 0−10%. The permeabilities, K, of water through the graphite plates with different porosity values were calculated by measuring the water flux over a range of pressures. The water permeability increased with oxidation and hydrophilization of the pore surface. Dynamic water contact angle measurements were used to characterize the effect of chemical and thermal treatments on the water wettability of the plates. The gas-breakthrough pressure of the water-infused plates was found to be linearly correlated with the parameter, $\gamma \cos\theta/\sqrt{K/\varepsilon}$, proportional to the capillary pressure of the gas−water interface of surface tension, γ, and contact angle, θ. Porous plates capable of a total water uptake greater than 25 wt %, with the gas-breakthrough pressure higher than 10 psi, through-plane electrical conductivity exceeding 100 S cm^{-1}, and flexural strength exceeding 25 MPa were obtained.

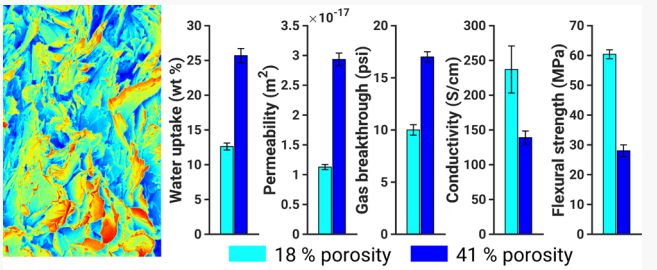

SEM image shows micropores (blue color) in graphite composite that can wick water. Increase in porosity increased water permeability but blocked gas leakage because of capillarity of the hydrophilic pores.

1. INTRODUCTION

Water management is a critical issue in low-temperature proton-exchange membrane (PEM) fuel cells designed to be operated under ambient conditions.[1−4] The proton-exchange membrane must be sufficiently hydrated to sustain high ionic conductivity. Conversely, excessive accumulation of water, referred to as the flooding of the fuel cell, is a significant problem that results in performance loss at low temperatures.[5] Water is produced at the cathode of the fuel cell due to the oxygen reduction reaction. Additionally, the protons transferred from the anode to the cathode bring along their water of hydration in a process called electro-osmotic drag.[6] Water is also introduced into the fuel cell by the humidified gas streams. Because of water accumulation by these processes, the gas flow channels that transport the reactant gases get flooded with water, causing intermittent power losses. The presence of liquid water in the gas flow channels or the gas-diffusion layer (GDL) can result in the inhomogeneous and discontinuous distribution of reactants over the active catalyst area, which not only affects the performance of an individual cell but also leads to cell-to-cell performance variations within a stack. Thus, water flooding of a fuel cell stack must be avoided by using proper water management strategies.

Several researchers have shown that surface modification of the flow channels to alter their water wettability can improve the fuel cell performance by avoiding water flooding.[7−11] Taniguchi and Yasuda[7] found that creating highly hydrophobic flow channels by surface roughening and plasma polymerization of hexafluoropropylene increased the peak power of the fuel cell under operating conditions that would otherwise lead to water accumulation. Owejan et al.[8] varied the geometry of the flow field (rectangular and triangular cross sections) and water wettability of the diffusion media to assess the overall volume and spatial distribution of accumulated water. They found that water accumulation was lower in a triangular

Received: May 7, 2021
Revised: June 24, 2021
Accepted: June 25, 2021

channel and when the channel surface was hydrophobic (with a water contact angle of 95°). Ge et al.[12] inserted strips of water-wicking materials in the gas flow channel. A poly(vinyl alcohol) (PVA) sponge, an absorbent cotton cloth, and an absorbent cotton paper were evaluated as the wicking materials. The PVA sponge, inserted in the cathode-side gas flow field, was more effective and resulted in a stable cell performance without external humidification of the reactant gases.

Modifications of the GDL, the microporous layer (MPL), and the membrane electrode assembly (MEA) for better water management have also been investigated.[13−17] Forner-Cuenca et al.[15] used GDLs with patterned wettability based on dip-coating the GDL with a hydrophobic fluorinated ethylene propylene polymer and local modifications of the polymer coating's wettability using radiation grafting of a hydrophilic monomer (*N*-vinyl formamide or acrylic acid). The hydrophilic pathways were intended to confine and remove water. Spernjak et al.[16] found that a hydrophilic MPL comprising aluminosilicate fibers and multiwalled carbon nanotubes improved water removal from the cathode catalyst layer, resulting in enhanced oxygen delivery to the electrocatalyst sites. However, they reported that the aluminosilicate fibers led to durability issues related to catalyst poisoning, caused by Al and Si dissolution and migration into the catalyst layer. Xiong et al.[17] studied a membrane electrode assembly that featured a bilayer structure for the cathode catalyst layer. The inner layer was a thin hydrophilic layer of perfluorosulfonate and the outer layer was a hydrophobic mixture of polytetrafluoroethylene (PTFE) and perfluorosulfonate. Using this MEA in combination with a hydrophobic MPL consisting of PTFE on the cathode-side gas-diffusion layer, they observed a non-monotonic dependence of current density (at a given cell voltage) on the PTFE concentration in the cathode catalyst layer. The current density increased with an increase in the PTFE concentration (indicating better water management) up to a particular PTFE concentration but decreased with a further increase in the PTFE concentration. Additionally, the cell performance showed a non-monotonic dependence on the MPL thickness as well.

Bipolar plates are components that connect adjacent cells in a fuel cell stack, into which the gas flow channels are machined or patterned. They can be made of metals,[18−20] but graphite bipolar plates are preferred because they are lighter and more resistant to corrosion.[21] Most prior studies[22−27] have focused on improving the electrical conductivity, flexural strength, acid resistance, and resistance to gas permeation of graphite bipolar plates. There are few studies that consider tailoring the porosity of bipolar plates for water removal.

Soleimani Alavijeh et al.[24] prepared bipolar plates using copper nanoparticles (0−5 wt %), natural flake graphite (22.5−17.5 wt %), and bisphenol A-based epoxy resin (77.5 wt %) and reported an ≅85% decrease in electrical resistance when the copper concentration was increased from 3 to 5 wt %. Kuan et al.[25] prepared bipolar plates using a woven graphite fabric cloth carbon coated with a phenol−formaldehyde resin as prepreg. For increasing electrical conductivity, graphite powder was added and mixed with the resin before applying it to the graphite cloth. Several layers of these prepregs were stacked into a mold and heated to obtain a composite laminate, which was subsequently carbonized at 600 °C. The average surface resistance decreased from about 203 mΩ/sq to about 36.7 mΩ/sq after carbonization. High-temperature carbonization was found to be necessary for an electrical conductivity higher than 100 S cm^{-1}. However, the flexural strength decreased from about 460 MPa to about 42 MPa after carbonization. Kahveci and Taymaz[26] coated the flow channels of graphite bipolar plates with polytetrafluoroethylene and silica using physical vapor deposition as the coating method. After the coating process, the water contact angles were 120° and 35° with PTFE and SiO_2, respectively. The highest current and power density values were obtained when the hydrophobic PTFE-coated plates were used in the PEM fuel cell stack tests. No voltage and current values could be measured due to excessive flooding of the flow channels in the SiO_2-coated bipolar plates. Alo et al.[27] reported the synthesis of graphite bipolar plates using a maleic anhydride-grafted polypropylene-compatibilized polypropylene/epoxy blend as the matrix. They found that the plate with 80 wt % graphite exhibited the optimal combination of flexural strength and electrical conductivity. The flexural strength was relatively high (≅40 MPa), but the through-plane conductivity was low (≅3.2 S cm^{-1}). The graphite plates in all of the above studies were nonporous, with low water absorption. For example, the water absorption of the graphite plates reported by Alo et al.[27] was in the range of 0.154% (at 30 wt % graphite) to 0.072% (at 70 wt % graphite).

The physicochemical modifications of the gas flow channels, GDL, MPL, and MEA described above are successful in alleviating water-management problems.[7−17] However, an alternative approach that does not block or hinder gas flow through the channels or slow mass transport of reactants to the catalyst layers, and allows direct removal of product water out of the fuel cell seems attractive, particularly in terms of maintaining the water mass balance in each cell (without relying solely on the thermodynamics of the water phase transformation and the kinetics of water production and transport through various parts of the system) and the ease of the cell stack assembly and its performance stability. A hydrophilic material in the gas flow channel, when fully hydrated, can block gas flow through the channel. The use of a porous bipolar plate would offer a more straightforward solution for water management in a PEM fuel cell. The product water can be removed from the fuel cell through the pores of the bipolar plate (into the coolant flow channels,[28] which are present in the bipolar plate besides the reactant flow channels), and the pore water can simultaneously humidify the reactant gas streams. In addition, the capillary pressure of the water-filled pores of tailored pore size and surface hydrophilicity would prevent gas leakage and keep the fuel (H_2) and air streams separated.

Gorman[29] reported the synthesis of porous graphite plates using a high-temperature (2000−3000 °C) carbonization process from constituents such as graphite powder, carbon fibers, phenolic resin, cellulosic fibers, and softwood pulp. However, such high-processing temperatures could make the resulting plates too expensive to be used as bipolar plates in automotive PEM fuel cells. Furthermore, their method does not provide a mechanism for porosity control. In the study reported herein, graphite bipolar plates were synthesized using graphite particles, phenolic resins, and pore-forming agents (porogens). Water-soluble compounds such as sucrose, sodium chloride, and poly(ethylene glycol) were used as sacrificial porogens to tailor the porosity of the plate. The porosity, water permeability, gas-breakthrough pressure, electrical conductivity, and flexural strength of the composite plates were

https://doi.org/10.1021/acs.iecr.1c01737
Ind. Eng. Chem. Res. XXXX, XXX, XXX−XXX

measured and correlated with their chemical composition and surface properties.

2. EXPERIMENTAL SECTION

2.1. Materials. Phenolic resin (resol phenol−formaldehyde resin, Plenco 12114, Plenco, Sheboygan, WI), graphite powder (surface-enhanced flake graphite 3775, Asbury carbons, ≥98% carbon), sucrose (Dominos sugar), sodium chloride (Fisher Scientific), poly(ethylene glycol) (Sigma-Aldrich, 10,000 g mol^{-1}), aqueous sulfuric acid (≅98%, BDH), and aqueous hydrogen peroxide (≅35 wt %, BDH) were used as received.

2.2. Methods. *2.2.1. Preparation of Porous Graphite Plates.* The phenolic resin powder (0.882 g) was dissolved in acetone (4 g). Sucrose (0.118 g) was dissolved in this solution, which was then transferred to a mortar containing the graphite powder (5.000 g). The mixture was ground to a paste and then spread to a uniform thickness in a 50.8 × 50.8 mm steel mold cavity. The steel mold surface was polished and mold release (E408 Dry Film Mold Release, Stoner, Quarryville, PA) was applied before compression molding. The paste was dried in a hot air oven at 60 °C for 8 h and molded in a hydraulic press with electrically heated platens (model 25-1515-2TMBX, Wabash MPI Carver, Wabash, IN) maintained at 170 °C for 20 min under a compressive pressure of 9.58 bars (clamping force of 10 US ton). The space above the oven and the compression molding press were ventilated using the laboratory's blower and duct system.

The surfaces of the compression-molded plate were polished by rubbing with aluminum oxide sandpaper (220 grit) to remove any impervious surface film of the polymer formed during compression molding. The thermally cured plate was immersed in hot water, maintained at 90 °C, for 60 min, to allow the water to percolate through the plate and extract the porogen. Finally, the plate was thoroughly washed with deionized water at room temperature and dried in an oven to a constant weight. The resulting plates were of ≅50 × 50 × 1.5 mm in dimensions.

Plates of other compositions were similarly prepared. Table 1 gives the compositions of the plates prepared using the phenolic resin. The masses of the phenolic resin are those of the polymer before thermal curing. Heating the resin during compression molding resulted in its cross-linking associated with mass loss (due to the evolution of water and formaldehyde, and the formation of methylene linkages), which was characterized using thermogravimetric analysis (TGA).

Table 1. Composition of Pastes Used for Preparing Porous Graphite Plates for the Porogen Concentration Variation Study

sample[a]	graphite (g)	polymer (g)	porogen (g)
90G-0P	5.400	0.600	0
85G-0P	5.100	0.900	0
80G-0P	4.800	1.200	0
85G-2P	5.000	0.882	0.118
85G-4P	4.904	0.865	0.231
85G-6P	4.811	0.849	0.340
85G-8P	4.722	0.833	0.444
85G-10P	4.636	0.818	0.546

[a]The sample name is based on the mass concentrations of graphite and porogen used in the preparation of the plate. For example, 85G-2P denotes a plate prepared using 85 wt % of graphite, 15 wt % of phenolic resin, and 2 parts of porogen for 100 parts of graphite and phenolic resin blend.

2.2.2. Surface Treatment of Pores. Aqueous solutions of hydrogen peroxide, and a mixture of hydrogen peroxide and sulfuric acid, were used as oxidants for the surface treatment of the porous graphite plates. The hydrogen peroxide solution was obtained by diluting 35 wt % hydrogen peroxide (50 mL) with deionized water (100 mL). The resulting solution contained ≅12.6 wt % H_2O_2. The solution of sulfuric acid and hydrogen peroxide was obtained by first adding sulfuric acid (98 wt %, 50 mL) to deionized water (50 mL) and then hydrogen peroxide (35 wt %, 40 mL) to this mixture. The resulting solution contained about 48 wt % H_2SO_4 and 8.5 wt % H_2O_2. The porous plates were soaked for 30 min in freshly prepared unstirred oxidant solutions at room temperature under vacuum (≅29 in Hg). They were then rinsed with DI water and dried in an oven at 60 °C at ambient pressure for 12 h before further characterization. Air oxidation was conducted in a muffle furnace (Lindberg/Blue M BF51848A) by heating at 250 °C for 30 min and 400 °C for 1 h.

2.2.3. Thermogravimetric Characterization of the Phenolic Resin Curing. TGA of the phenolic resin was carried out using a Discovery TGA55 thermogravimetric analyzer (TA Instruments, New Castle, DE) to characterize its mass loss during thermal curing. The resin was dried in a vacuum oven at 60 °C for 8 h, a 20−30 mg aliquot of which was heated in a Pt pan at a constant heating rate of 20 °C min^{-1} under a nitrogen gas purge at a flow rate of 25 cm^3 min^{-1} (standard ambient temperature and pressure). Isothermal TGA measurements were carried out at 170, 250, and 400 °C for temperature holding times of 20, 30, and 60 min, respectively. The heating rate to attain these temperatures was 20 °C min^{-1}. The mass loss measurements were performed under both nitrogen (flow rate of 25 cm^3 min^{-1}) and air (flow rate of 5 cm^3 min^{-1}).

2.2.4. X-ray Photoelectron Spectroscopy. Samples were analyzed using a Scienta Omicron ESCA-2SR with an operating pressure of ≅1 × 10^{-9} Torr. Monochromatic Al Kα X-rays (1486.6 eV) were generated at 250 W (15 kV, 20 mA), and photoelectrons were collected from a 2 mm diameter analysis spot at a 0° emission angle. The source to analyzer angle was 54.7°. A hemispherical analyzer determined the electron kinetic energy, using a pass energy of 200 eV for survey scans and 50 eV for high-resolution scans.

2.2.5. Porosity Measurement. A specimen of the graphite plate was dried in an oven at 60 °C. After cooling to room temperature in a desiccator, its mass, m_1, was determined using an analytical balance (Mettler Toledo, model XS64). Next, the plate was submerged in deionized water at ambient pressure and temperature for 10 min, removed from the water, lightly dabbed using a lint-free paper (Kimwipes) to remove water droplets adhering to the surface, and weighed to obtain the mass, m_{2a}, of the plate saturated with water at ambient pressure. Finally, the plate was submerged in water taken in a Petri dish, which was placed in a vacuum chamber (Lindberg/Blue M 18.6 L vacuum oven, 1 Torr capacity) connected to a vacuum pump (Welch DuoSeal) at room temperature. The port of the oven connected to the pump was slowly opened until the vacuum gauge indicated a maximum reading of 30 inHg. The mass, m_{2v}, of the plate after this 10 min vacuum-driven water-infusion process was determined using an analytical balance. Subsequently, this plate was suspended in water by placing the specimen in a wire loop, and its mass, m_3,

https://doi.org/10.1021/acs.iecr.1c01737
Ind. Eng. Chem. Res. XXXX, XXX, XXX−XXX

while suspended in water, was determined. Before measurement, the microbalance was tared by immersing the wire loop to the same depth as was used when the specimen was in place.

The plates infused with water at ambient pressure are called "wick-filled," and those infused with water under a vacuum are referred to as "vacuum-filled."

2.2.6. Gas-Breakthrough Pressure. For determining the gas-breakthrough pressure of the porous plates, the permeability cell shown in Figure 1 was used. Porous graphite plate 1

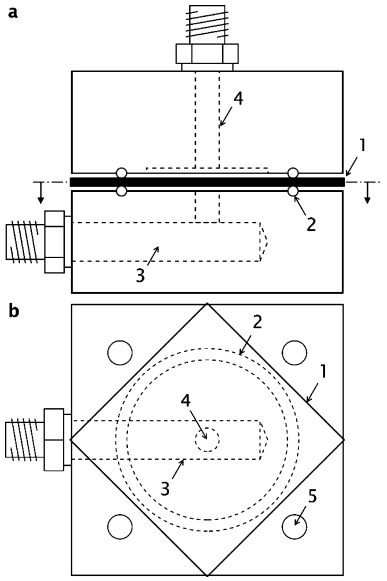

Figure 1. (a) Side view and (b) top view of the section shown by the dashed-dotted line in (a) of the permeability cell used for the measurement of gas-breakthrough pressure and water permeability. 1—graphite plate specimen; 2—rubber O-ring; 3—channel in the bottom holder; 4—channel in the top holder; and 5—one of the four bolt holes in each of the bottom holder and top holder.

was assembled between the bottom and top parts of the cell, sealed with rubber O-rings 2, one on each side of the plate, and clamped using steel bolts. The bottom part contained gas inlet channel 3 and the top part consisted of exit channel 4. The inlet port was connected to a compressed air source with a pressure gauge in between. The exit channel was filled with water. The air pressure at the inlet was increased in steps, in the range of 0—30 psi relative to atmospheric pressure, until the passage of air through the plate was evident in the form of a bubble at the exit port. This pressure was recorded as the gas-breakthrough pressure. The gas-breakthrough pressure measurements were made for wick-filled and vacuum-filled plate specimens. Measurements on four identical plates were used to determine the average and standard deviation (reported as uncertainty).

2.2.7. Water Permeability Measurement. The assembly shown in Figure 1 was also used to measure the water permeability of the porous plate specimens. Pressurized water was supplied to the plate specimen using channel 4, and the permeate was collected through channel 3. The flow area, defined by the size of the O-rings, was ≅13.42 cm^2. The permeability cell was connected to a water tank, a diaphragm pump (Hydra-Cell, model F20-X), a pulsation dampener (Blacoh, model H1120V-5), and a pressure gauge, as shown in Figure 2. The pump was operated at a speed of 1000 rpm, and the pressure difference, ΔP, across the plate thickness (the

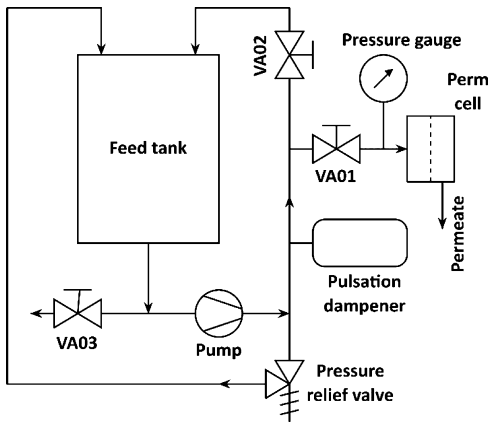

Figure 2. Experimental setup for permeability measurement.

pressure in channel 4 minus the pressure in channel 3, which was equal to the atmospheric pressure) was adjusted using a needle valve VA01 (Swagelok, Model SS-1RS4) to be in the range of 0.69—4.14 bar (10—60 psi). The water that permeated through the porous plate was collected for flow rate measurement. For each pressure difference, the mass of the permeate collected over 5 min was used to calculate the permeate mass flow rate, which was converted to the volumetric flow rate using water density. Permeate flow rate measurements showed that a steady state was reached within 5 min of changing the feed flow rate. Therefore, 5 min was allowed between each increment in pressure and the measurement of the permeate flow rate.

2.2.8. Water Contact Angle. Dynamic contact angle measurements were performed using a contact angle goniometer (model 100-00, Ramé-Hart, Netcong, NJ) using water as the probe liquid and a 22-gauge blunt tip stainless-steel needle (0.7 mm o.d. and 0.4 mm i.d.).

2.2.9. Electrical Conductivity. For the measurement of through-plane electrical conductivity, the graphite plate specimen, whose length, l, width, w, and thickness, t, were measured using a caliper, was placed in between two gold-coated copper electrodes (see Supporting Information). On each side of the plate, carbon cloth (Zoltek Panex PX30 PW06 woven carbon fiber fabric, Fuel Cell Store, TX) was inserted between the graphite plate and the metal electrode to ensure good electrical contact of the metal electrode with the test specimen. The entire assembly was clamped in a press under a compressive load of 1000 kgf, and the voltage drop across the thickness of graphite-plate/carbon-cloth assembly was measured for currents in the range of 0.1—1.0 A. The current was applied using a digital DC power supply (model 3006, Protek Power NA, Hudson, MA), and the voltage was measured using a digital nanovoltmeter (model 2182A, Keithley Instruments, Cleveland, OH). The measurements were repeated for the carbon cloth without the graphite plate in between. The slopes of the linear fits of voltage versus current data gave the resistance, R_1, of the graphite-plate/carbon-cloth assembly and the resistance, R_2, of the carbon cloth. Assuming that the total resistance, R_1, is the sum of the resistances of the graphite plate and the carbon cloth, the resistance, R, of the graphite plate was calculated using $R = R_1 - R_2$, from which the plate conductivity, κ, was obtained using

$$\kappa = \frac{t}{Rlw} \tag{1}$$

https://doi.org/10.1021/acs.iecr.1c01737
Ind. Eng. Chem. Res. XXXX, XXX, XXX—XXX

2.2.10. Flexural Strength Measurement. The flexural modulus and flexural strength of the composite specimens were characterized by a three-point bending method using a 5900R Universal Testing System (Instron, Norwood, MA). A specimen of the graphite plate, of rectangular cross section (≅50 mm long, 12.5 mm wide, and 1.5 mm thick), was mounted on a three-point bend clamp (3PT bend fixture with 10 mm anvils, Instron OP336-42), and tested following the ASTM D790 standard.[30] The width and thickness of the specimen were measured at the center of the support span using a caliper. The displacement of the center point was carried out at a rate of 0.1 mm min^{-1}. The cross-head position was used for the displacement measurement. For each material composition, at least two different plates were tested, and the reported values of yield strength, flexural modulus, and flexural strength are averages of these measurements.

3. RESULTS AND DISCUSSION

3.1. Processing Temperature for Porous Graphite Composite Plate Preparation. The porous bipolar plates of the present work were prepared using graphite powder (80−95 wt %), a polymer binder (5−20 wt %), and a porogen, such as table salt, sugar, or poly(ethylene glycol), in a concentration of 0−10 % of the combined mass of the graphite and polymer (see Table 1). The Plenco 12114 phenolic resin, received as a solid powder soluble in acetone, was used as the polymer binder. The Asbury 3775 surface-enhanced flake graphite had a surface area of 24 m^2 g^{-1}, which is higher than that of natural flake graphite (≅13 m^2 g^{-1}) because of thinner flakes.

Plenco 12114 is a resol-type phenolic resin. Resol phenolic resins are obtained by a base-catalyzed reaction of a stoichiometric excess of formaldehyde with phenol (typically a molar ratio of 2:1),[31,32] so that there is a sufficient number of methylol groups (Figure 3a), which remain reactive to thermally cure the resin without the incorporation of an additional cross-linking agent.[33] Figure 4 shows the result of the thermogravimetric analysis of the resin used in the synthesis of the graphite plates. Peaks in the mass loss rate were observed at temperatures of 98, 172, 234, and 570 °C (cf. Figure 4a). The first three are attributed to the thermal curing

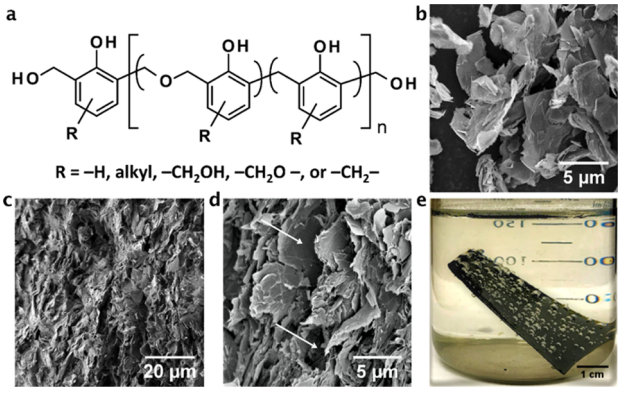

Figure 3. (a) Chemical structure of a resol resin. (b) SEM image of graphite particles (Asbury 3775). (c,d) SEM images of the cross section of a compression-molded graphite plate at two different magnifications; large-sized pores are marked by arrows. (e) Photograph of a compression-molded plate immersed in water at 90° C for the removal of the porogen. Air bubbles at the surface and the color change of water (due to the removal of the sucrose porogen) indicate the pore formation.

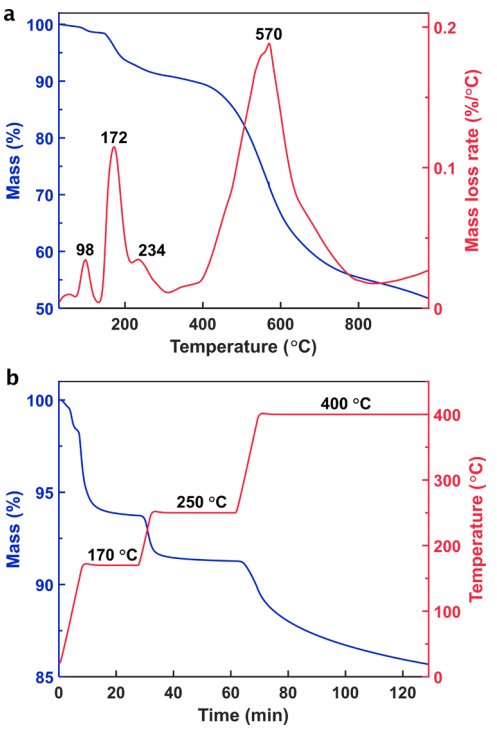

Figure 4. (a) Thermogravimetric analysis of phenolic resin at a constant heating rate of 20 °C min^{-1} under a nitrogen gas flow rate of 25 cm^3 min^{-1} (b) Isothermal TGA measurements of mass loss vs time at graphite-plate-processing temperatures of 170, 250, and 400 °C.

reactions of the $-CH_2OH$ groups, involving the loss of water and formaldehyde (resulting in the formation of methylene cross-links), and the reaction at 570 °C is attributed to the thermal degradation of the polymer. A detailed discussion of the infrared spectroscopy results for the phenolic resin cured at different temperatures is given in the Supporting Information. Figure 4b shows that the mass loss was ≅6% at the end of the isothermal heating step at 170 °C, ≅9% after heating at 250 °C, and ≅14% after heating at 400 °C. Therefore, it is expected that the thermal treatment of the plate at 400 °C would increase its porosity by partial removal of the resin.

The porosity, permeability, electrical conductivity, and flexural strength of graphite−polymer composite plates prepared by hot pressing at 170 °C were compared with those prepared by hot pressing at 170 °C and subsequent heating at 250 °C (30 min) and 400 °C (1 h). The effects of porogen type and concentration were similarly investigated.

3.2. Porosity. The use of sacrificial porogen is a highly promising method of introducing porosity in materials. Amnuaypanich and co-workers used porous sugar cubes as templates for preparing porous polydimethylsiloxane (PDMS) sponges.[34] In their approach, a solution of the polymer, the cross-linker, and the catalyst was poured on the sugar cubes, and the sugar cubes soaked with this solution were thermally cured to form the PDMS network. Then, the sugar template was dissolved in water, leaving behind the porous PDMS gel.

In contrast, the method used in the present study involves blending the porogen, which can even be liquids such as poly(ethylene glycol), with the composite materials. Our approach allowed facile control of porosity by varying the concentration of the porogen in the blend (*vide infra*), which is difficult in other methods of preparation of porous graphite plates such as high-temperature carbonization.[29]

https://doi.org/10.1021/acs.iecr.1c01737
Ind. Eng. Chem. Res. XXXX, XXX, XXX−XXX

The porosity of the plates was characterized by a procedure similar to that reported in the ISO 10545-3 standard.[35] In the present study, wick-fill mass gain, E_w, is defined as the relative increase in the mass of a predried porous plate because of the penetration of water into the plate by wicking at atmospheric pressure. It is expressed as a percentage of the dry mass using

$$E_w = \frac{m_{2a} - m_1}{m_1} \times 100 \quad (2)$$

The vacuum-fill mass gain, E_v, is defined as the relative increase in the plate mass because of the penetration of water into the plate in vacuum. It is calculated using

$$E_v = \frac{m_{2v} - m_1}{m_1} \times 100 \quad (3)$$

E_w represents water penetration into the easily fillable pores, and E_v represents penetration into almost all of the open pores. Consistent with the definitions in the ISO standard, the total (external) volume, V, of the plate was obtained using

$$V = \frac{m_{2v} - m_3}{\rho_w} \quad (4)$$

and the volumes of the open pores, V_o, and the impervious portion, V_i, were calculated using

$$V_o = \frac{m_{2v} - m_1}{\rho_w} \quad (5)$$

and

$$V_i = \frac{m_1 - m_3}{\rho_w} \quad (6)$$

ρ_w is the density of water. The porosity, ε, is the ratio of the volume of the open pores of the test specimen to its exterior volume.

$$\varepsilon = \frac{V_o}{V} \quad (7)$$

The specific volumes, v, v_o, and v_i, were computed by normalizing V, V_o, and V_i by the mass, m_1, of the dry plate.

Figure 5 shows the wick-fill and vacuum-fill mass gains, E_w and E_v, respectively, of three different water-soluble porogens: sucrose, sodium chloride, and low-molecular-weight PEG. Higher values of E_w and E_v correspond to higher plate porosity. The use of sucrose resulted in the largest mass gain and it was used as the porogen for the subsequent studies reported herein. Unlike sodium chloride, sucrose melts and undergoes a chemical transformation when heated to 170 °C, the temperature of the compression-molding process. However, the data in Figure 5 show that the sugar byproducts can be removed from the graphite plate leaving behind pores. The slightly lower water uptake (porosity) of the graphite plates prepared using sodium chloride is attributed to the higher density of sodium chloride than sucrose (2.16 vs 1.59 g cm^{-3}, respectively). At the same mass concentration, sucrose would occupy about 36% higher volume in the composite than sodium chloride. Although the room-temperature density of PEG is lower than even that of sucrose, the relatively high molar mass and high viscosity of PEG would hinder its removal from the plate, resulting in a lower porosity (and a lower E_v) compared with sucrose.

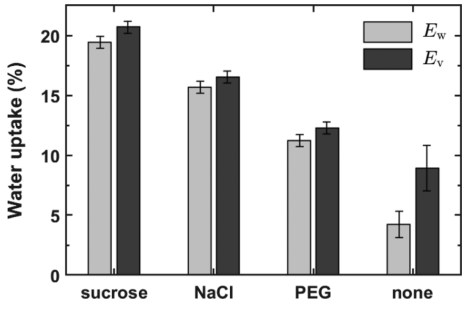

Figure 5. Variation of wick-fill mass gain, E_w, and vacuum-fill mass gain E_v, for plates prepared using different water-soluble porogens. The plates were molded using graphite and the phenolic resin in a mass ratio of 82:18, respectively. The mass of porogen was 2% of the total mass of the graphite and the resin.

Figure 6a shows the variation of E_v with the porogen concentration. E_v increased, almost linearly, with an increase in the concentration of sucrose used in the synthesis. Figure 6b shows the variations in the total, impervious, and open-pore specific volumes. The total specific volume, v, was almost independent of the porogen concentration, as expected. The slight decrease in v with an increase in the sucrose concentration is likely because of the formation of a more compact packing of graphite and phenolic resin in the composite due to the plasticization effect of molten sucrose. The significant decrease in the impervious volume (conversely, an increase in the open pore volume) indicates the increase in the porosity of the plate (calculated using eq 7) with an increase in the porogen concentration, as seen in Figure 6c.

3.3. Water Permeability. The volumetric flow rate, Q, of a fluid with viscosity, η, across a porous material of the cross-sectional area, A, and thickness, t, is given by Darcy's law

$$Q = \frac{KA\Delta P}{\eta t} \quad (8)$$

where ΔP is the pressure difference between the two sides of the plate, t is the plate thickness, and K is the material's permeability. A steady-state measurement of Q for a given $\Delta P/t$ would yield the permeability of the measurement. However, to account for capillary end effects and the pressure gauge's zero offset,[36] steady-state measurements were conducted at several pressure gradients. The Q versus $\Delta P/t$ data for the graphite plates of the present study were found to be linear and were corrected for a non-zero intercept by using a constant additive correction for ΔP (of ≅9 psi for all the specimens), which does not affect the slope of the curve (and therefore the permeability).

The water permeability of the graphite plates prepared with and without using the sucrose porogen (samples 85G-0P and 85G-10P; cf. Table 1 for the plate compositions) was determined by measuring water flow rates for different pressure gradients across the plate thickness. Graphite plates, whose pore surfaces were made hydrophilic by treatment with the oxidizing agents, aqueous H_2O_2 and H_2SO_4 + H_2O_2 solutions, at room temperature, and plates heated in air at a temperature of 400 °C (below the autoignition temperature of graphite, ≅730 °C) for 1 h were also evaluated. Figure 7a shows good fits of the Q/A versus $\Delta P/\eta t$ data to a linear model, in excellent agreement with Darcy's law (coefficient of determination, R^2, for the linear correlation >0.99 in all cases).

As observed in Figure 7a, the permeate flux for a given pressure gradient was higher for the plates prepared using the sucrose porogen (85G-10P) than the plate prepared without

https://doi.org/10.1021/acs.iecr.1c01737
Ind. Eng. Chem. Res. XXXX, XXX, XXX−XXX

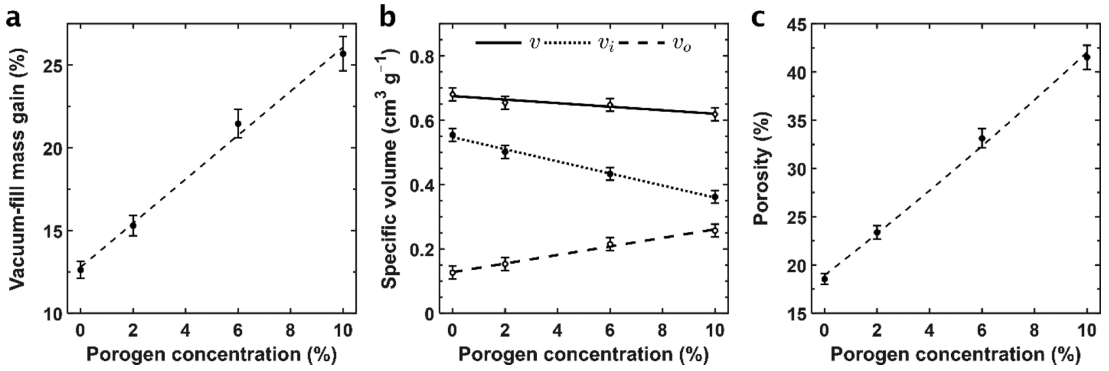

Figure 6. Effect of porogen concentration on the (a) vacuum-fill mass gain, E_v, (b) total specific volume, v, impervious volume, v_i, and open pore volume, v_o, and (c) porosity. Data shown are for the 85G-0P, 85G-2P, 85G-6P, and 85G-10P plates (see Table 1).

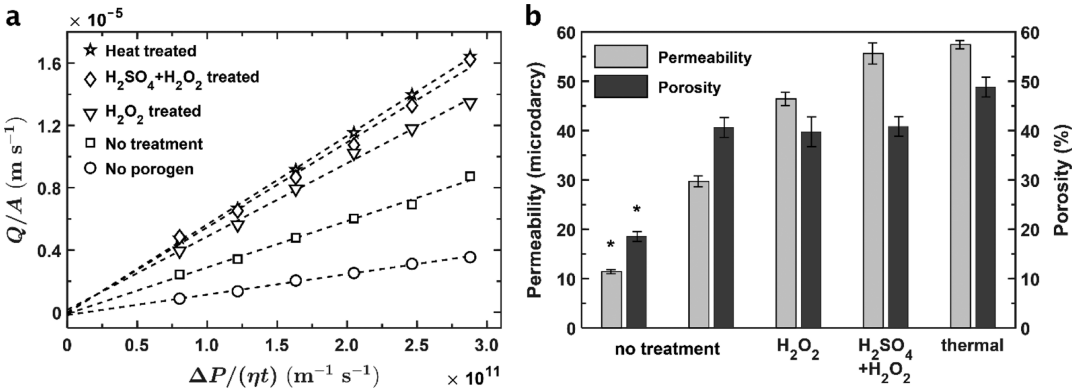

Figure 7. (a) Water permeability data for the graphite plates prepared without using a porogen (85G-0P, ○) and with 10% of sucrose porogen (85G-10P, □). Data for porous plates prepared using 10% porogen and treated with aqueous H_2O_2 solution (▽) and H_2SO_4 + H_2O_2 solution (◇), or heated in air at 400 °C for 1 h (☆) are included as well. The flow rate, Q, was normalized by the constant flow area, A, to obtain the superficial velocity of the permeate flow. The pressure gradient, $\Delta P/t$, was divided by the room-temperature viscosity of water ≅1 × 10^{-3} Pa s. Slopes of the linear fits of data yield the permeability values of the plate. (b) Permeability and porosity of 85G-0P and 85G-10P graphite plates prepared using different oxidative treatments. Permeability values are reported in units of darcy (D). The SI unit for permeability is m^2. 1 μD = 9.869 × 10^{-19} m^2. * indicates data for 85G-0P. All other data are for the 85G-10P specimens.

the porogen (85G-0P). Furthermore, the plates with the pore surfaces rendered more hydrophilic by oxidation yielded higher permeate flux values. Figure 7b shows a comparison of the permeability of these plates. A permeability of 1 darcy corresponds to the flow of 1 cm^3 of a fluid with a viscosity of 1 cP across an area of 1 cm^2 through a medium with a thickness of 1 cm under a pressure difference of 1 atm.

The water permeability increased from about 11 μD for the graphite plate prepared without using a porogen to about 30 μD for that prepared using 10% sucrose. The oxidation of the pore surface using aqueous H_2O_2 and H_2SO_4 + H_2O_2 resulted in increased permeabilities of 46 and 56 μD, respectively. The oxidation of the pore surface by heating in air resulted in a permeability of about 57 μD.

Figure 7b also shows the porosity of the plates determined using the dry mass, water-filled mass, and the suspended mass of the plates. The permeability of a medium depends on the porosity of the plate. According to the Kozeny−Carman equation, permeability is proportional to $\varepsilon^3/(1-\varepsilon)^2$. However, the Kozeny−Carman equation applies to porous media of different porosities, particle sizes, and shapes but does not account for differences in surface wettability. It is seen from Figure 7b that the porosity of 85G-10P remained practically unaffected by treatment using aqueous H_2O_2 and H_2SO_4 + H_2O_2 solutions. From the masses of the plates recorded before and after the surface-oxidation process, the mass loss was found to be comparable for the H_2O_2 solution and H_2SO_4 + H_2O_2 solution treatments (about 2.6 and 3.9 wt %, respectively) and higher (about 7.8 wt %) for the thermal treatment. However, the permeability of the untreated 85G-10P plate was significantly lower than those of the H_2O_2- and H_2SO_4 + H_2O_2-treated plates. The difference in the permeabilities of these three plates cannot be accounted for using the Kozeny−Carman approach. Indeed, R^2 for a linear fit of K versus $\varepsilon^3/(1-\varepsilon)^2$ was low (≅0.04). An analysis that considers the effects of the differences in the interfacial energy of water and the pore surface, and therefore, the capillary pressure, is required.

3.4. Surface Wettability and Capillary Pressure. Free-standing graphene is hydrophilic with a water contact angle, θ_w, of 42°.[37] However, graphite, which contains stacked graphene layers, has a higher θ_w value. The water contact angle of highly oriented pyrolytic graphite (HOPG) is found to be in the range of 60−92°.[38−41] For crystalline graphite, Fowkes and Harkins[42] reported a θ_w of 85.6 ± 0.3° and a dispersion component of the surface energy, γ_s^d, equal to 109 mJ m^{-2};[43] Morcos reported a θ_w of 84.2° and γ_s^d of 110.6 mJ m^{-2};[44] and Kang and Li[45] reported θ_w to be in the range of 86−90°. Wang et al.[46] also reported a relatively high θ_w of 98 ± 5°, but their value of a surface energy of 58.4 mJ m^{-2} is significantly lower

https://doi.org/10.1021/acs.iecr.1c01737
Ind. Eng. Chem. Res. XXXX, XXX, XXX−XXX

than the values reported by Fowkes[43] and Morcos.[44] Nevertheless, most other studies indicate that graphite is a high surface energy material (with a high dispersion component) with a hydrophobic surface, even though graphene may be hydrophilic. Hence, the introduction of polar surface functionalities (such as hydroxyl or carboxyl groups) would be required to make the pores in our graphite plates wettable by water.

All of the graphite plates exhibited a large water contact angle hysteresis, as seen in Figure 8. The advancing contact angle for all the plates, except the thermally air-oxidized plate, was greater than 90°, indicating a hydrophobic surface characteristic of graphite. In contrast, the receding water contact angles for all porogenated plates, including those that were not surface-treated, were fairly low, below 30°, indicating hydrophilic surfaces resulting from the water uptake by the pores and the introduction of polar hydroxyl and carboxyl groups on the surface because of the oxidation treatment. The contact angle of the thermally treated plate is significantly lower because of a higher porosity (introduced by a greater extent of thermal degradation and volatilization of the relatively hydrophobic phenolic resin; cf. Figure 4b) in addition to the surface oxidation of graphite. The X-ray photoelectron spectroscopy results shown in Figure 9 confirm the presence of polar groups on the surface-treated plates.

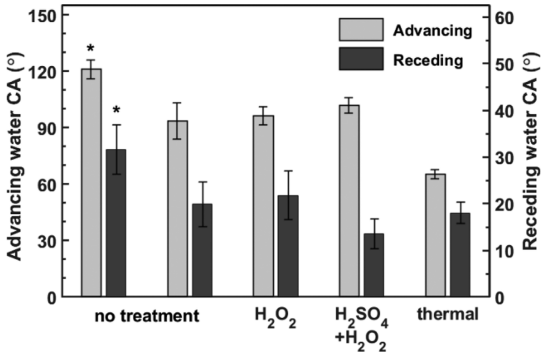

Figure 8. Advancing and receding contact angles of water on untreated and surface-treated 85G-10P graphite plates. Data for 85G-0P prepared without using a porogen are also shown (and indicated by asterisks).

Based on the relative intensities of the C 1s and O 1s peaks in the survey scan (at binding energy values of approximately 284 and 533 eV, respectively), the oxygen concentration was found to be about 4 atom %. The C 1s spectrum was fitted using the characteristic asymmetric peak for the sp^2 carbon atoms at 284.2 eV, along with symmetric loss peaks. The symmetric loss peaks were located at 289.5, 291.4, and 293.9 eV, respectively. The total intensity of these three peaks was 10% of the C 1s peak intensity. In addition, peaks corresponding to C−O and C(═O)−O carbon atoms were found at 285.7 and 288.3 eV. The intensity of these two peaks, resulting from the oxidized carbon atoms, was about 12% of the total intensity under all peaks observed in the C 1s spectrum. The higher number of oxidized carbon atoms, inferred from the C 1s spectrum, than the number of oxygen atoms, indicated by the survey scan, suggests that the polar oxygenated groups are present deeper within the XPS probe

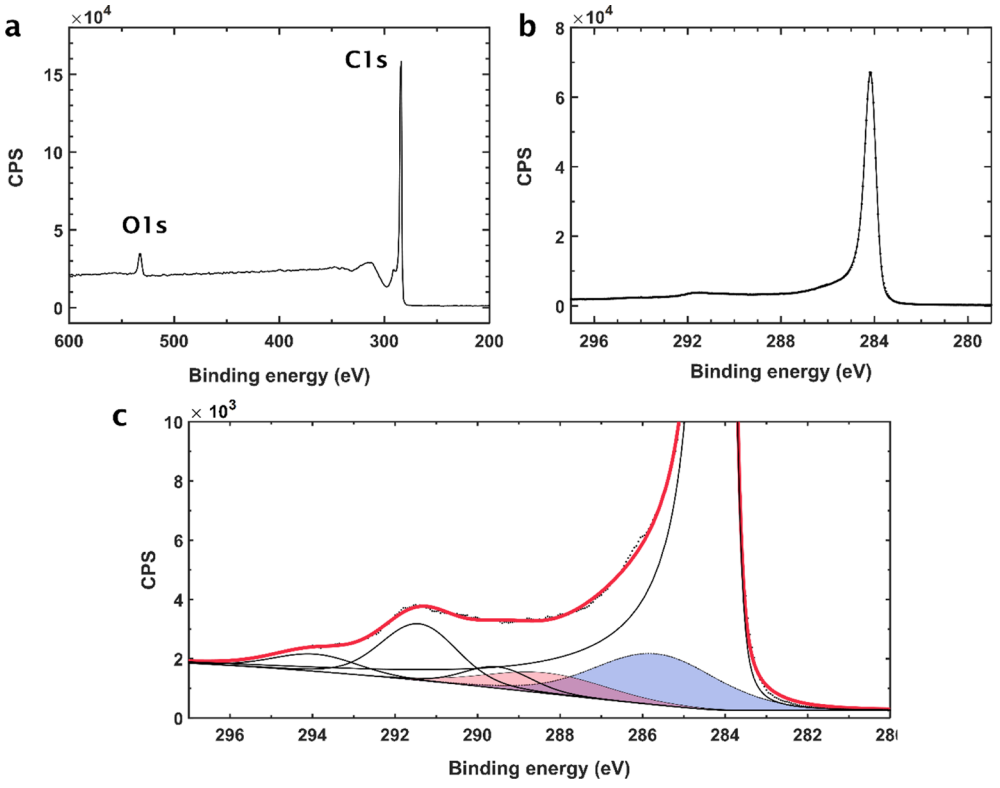

Figure 9. (a) Survey scan of the graphite plate oxidized by heating in air. (b) High-resolution C 1s XPS spectrum. (c) Peak fitting of the C 1s spectrum. The discrete points represent experimental data of counts per second (CPS) vs binding energy, and the curves represent fitted peaks. The peaks colored blue and red correspond to C−O and C(═O)−O carbon atoms and the remaining four peaks (one asymmetric peak and three symmetric peaks) are characteristic of pristine graphite.

https://doi.org/10.1021/acs.iecr.1c01737
Ind. Eng. Chem. Res. XXXX, XXX, XXX−XXX

depth ($\lesssim$ 10 nm, depending on the inelastic mean free path of the photoelectrons through graphite, which is ≅3.1 nm for the C 1s photoelectrons with a binding energy of 284.2 eV, and hence a kinetic energy of ≅1202.4 eV). Regardless, it is evident from these results that about 4 to 14 % of the C atoms in the top few nanometers of the plate surface are oxidized. The decrease in the water contact angle after oxidation is attributed to the presence of these oxidized carbon atoms (which, if present in excessive concentrations, would decrease the plate's electrical conductivity).

The low receding contact water angles indicate the hydration of the plate surface because of the binding of water to the polar functional groups on the plate surface and water absorption by the pores present on the surface. However, no significant decrease in the water droplet size was observed on a macroscopic scale during dynamic contact angle measurements (over a time scale of about 1 min). Although the surfaces of the plates would be nonhomogeneous because of the presence of pores, the effects of compositional heterogeneity or surface roughness (such as the pinning of the contact line) were generally not observed. The contact line of the droplet with the surface advanced or receded smoothly on the surface, without pinning, on all the test samples. In the few cases where pinning was observed (<2% of the measurements), these data were excluded from further analysis. The MATLAB function *rmoutliers* (The MathWorks, Inc.) was used to detect and remove outliers, defined as values that are more than three scaled median absolute deviations away from the median. The root-mean-square roughness (determined over a surface area of ≅9 × 12 mm using a non-contact optical surface profiling technique) was 3.0 μm for 85G-0P prepared without using a porogen, 3.3 μm for 85G-10P prepared using 10% of sucrose porogen, and 4.2 μm for 85G-10P after thermal treatment at 400 °C (cf. Supporting Information).

For the calculation of capillary pressure, the cosine of the contact angle was calculated as the average of the cosines of the advancing and receding contact angles, based on the equation of Kamusewitz and Possart for Wenzel's model of a rough surface.[47]

$$\cos \bar{\theta} = \frac{\cos \theta_a + \cos \theta_r}{2} \tag{9}$$

Using this equation, the average contact angle, $\bar{\theta}$ was ≅80° on 85G-0P. $\bar{\theta}$ was in the range of 65 ± 5° for the untreated 85G-10P, the H_2O_2-treated 85G-10P, and 85G-10P treated with the H_2SO_4 and H_2O_2 mixture. The graphite plate oxidized by thermal treatment in air showed the lowest $\bar{\theta}$ of ≅47°. A lower water contact angle is beneficial in terms of increasing the capillary pressure and exerting a greater resistance for gas leakage through the plate, as discussed in the following section.

3.5. Gas-Breakthrough Pressure. Figure 10a shows the experimentally determined gas (air)-breakthrough pressure, ΔP_g, the minimum pressure required for a gas to break the liquid seal and pass through the plate. For all plates, ΔP_g was slightly higher for a vacuum-filled plate than the wick-filled plate, which is expected because vacuum-driven infusion would fill even the narrowest pores in the material. However, the difference between wick-fill and vacuum-fill breakthrough pressures is not large, indicating that the plates would be effective as gas barriers in practical applications at ambient pressures.

Interestingly, the ΔP_g values were higher for all the plates prepared using 10% sucrose porogen (and with higher porosity) than the plate composition that did not use the porogen (with lower porosity). This increase in ΔP_g and the improved sealing against the gas permeation of the more porous plates is attributed to the positive capillary pressure exerted by the water-filled pores in the porogenated plate.

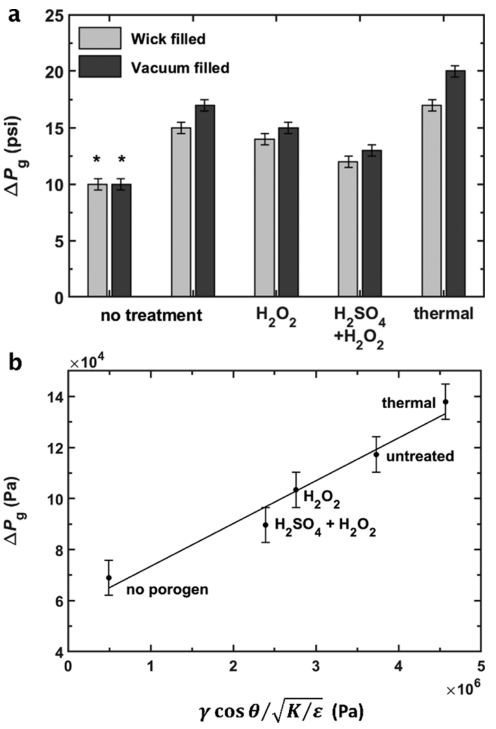

Figure 10. (a) Wick-fill and vacuum-fill breakthrough pressures for porous graphite plates of Figure 7. * denotes data for 85G-0P, while the other bars correspond to the 85G-10P specimens. (b) Plot of the vacuum-fill gas-breakthrough pressure vs the capillary pressure factor, $\xi = \gamma \cos \theta / \sqrt{K/\varepsilon}$. The average contact angle, $\bar{\theta}$, defined by eq 9, was used for θ. A surface tension, γ, of 72 mN m^{-1} was used for water at room temperature.

The capillary pressure, P_c, for a tube of radius, r, is given by Laplace's law

$$P_c = \frac{2\gamma \cos \theta}{r} \tag{10}$$

where γ is the surface tension of the liquid and θ is the contact angle of the liquid with the pore surface.

The capillary pressure will be positive for a hydrophilic surface (contact angle, θ < 90°) and negative for a hydrophobic surface (θ > 90°). For the contact angle of water with the pore surface, we used the contact angle of a water drop with the external flat surface of the plate. Although the advancing contact angles, θ_a, of the graphite plates were greater than 90° (cf. Figure 8), the average contact angle, $\bar{\theta}$, was below 90° for all the plates. Therefore, the water-filled pores of the graphite plates will resist the passage of the gas through the plate; ΔP_g would increase with an increase in the capillary pressure, P_c, which is inversely proportional to the pore size, r, and directly proportional to the hydrophilicity of the pore surface (quantified by cos θ).

For a complex porous medium with non-cylindrical pores, such as the plates of the present study (cf. Figure 3d), the radius of the pores is challenging to measure directly. Therefore, we used an approach based on the Leverett *J*-

https://doi.org/10.1021/acs.iecr.1c01737
Ind. Eng. Chem. Res. XXXX, XXX, XXX−XXX

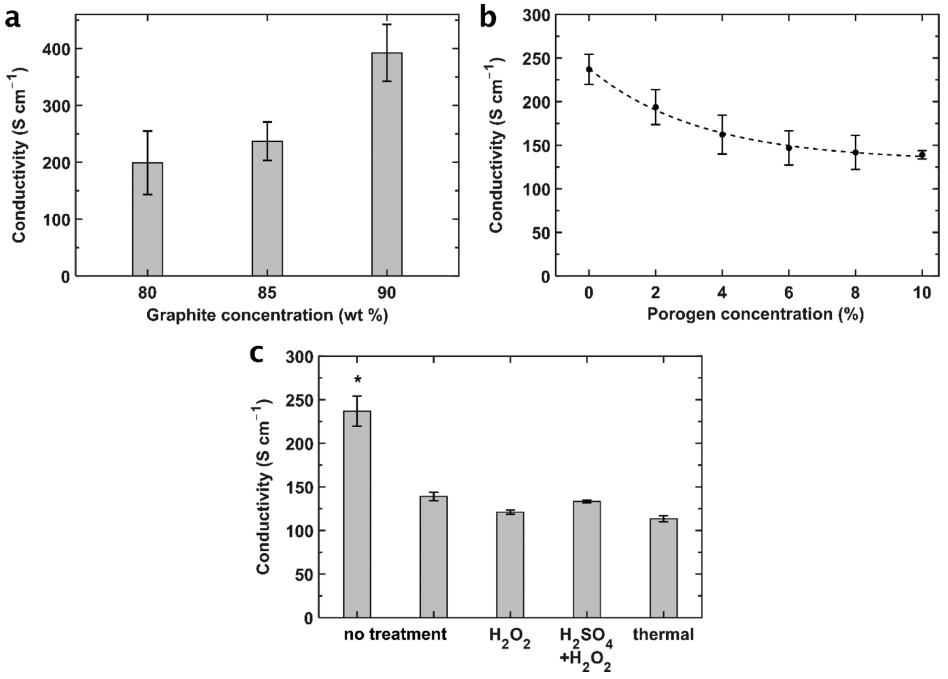

Figure 11. Electrical conductivity of graphite plates prepared using (a) different concentrations of graphite without using a porogen, (b) 85 wt % graphite and different concentrations of sucrose porogen, and (c) surface treatment by various oxidation methods. All measurements were at room temperature. The error bars denote standard uncertainty in conductivity measurements. Data in panel (c) are for the 85G-10P specimens, except the first bar marked by *, which corresponds to 85G-0P.

function[48] in the analysis of our data. In this approach, r for a porous medium is assumed to be proportional to $\sqrt{K/\varepsilon}$.

The Leverett J-function defined as

$$J = \frac{P_c}{\gamma \cos\theta}\sqrt{\frac{K}{\varepsilon}} \tag{11}$$

is used to characterize the permeability of porous media in petroleum engineering. Xu et al.[49] have provided a derivation of the J-expression using the Poiseuille equation for the relationship between the volumetric flow rate, Q, and the pressure drop, ΔP, for the flow through a bundle of n capillary tubes, each of length, l_1, and radius, r

$$Q = \frac{n\pi r^4}{8\eta l_1}\Delta P \tag{12}$$

The porosity of the capillary bundle can be written as the ratio of the total volume, $n\pi r^2 l_1$, of the tubes, to the volume, Al_1, where A is the cross-sectional area of the bundle.

$$\varepsilon = \frac{n\pi r^2}{A} \tag{13}$$

The permeability of the capillary bundle, according to Darcy's law, is

$$K = \frac{Q\eta l_2}{A\Delta P} \tag{14}$$

where l_2 is the thickness of the bundle. Equations 13 and 14 give an expression for K/ε containing $Q\eta/\Delta P$ that can be written in terms of the pore geometry alone using eq 12. Thus,

$$r = \sqrt{\frac{8l_1}{l_2}\left(\frac{K}{\varepsilon}\right)} \tag{15}$$

which along with eq 10 is the basis for the $\sqrt{K/\varepsilon}$ term in the Leverett J parameter. The ratio, l_1/l_2, is the tortuosity, τ, of the tube bundle.

Figure 10b shows a plot of the vacuum-fill air-breakthrough pressure versus the parameter, ξ, given by

$$\xi = \frac{\gamma \cos\overline{\theta}}{\sqrt{K/\varepsilon}} \tag{16}$$

An excellent linear correlation ($R^2 \cong 0.96$) was observed for the data set. The slope of the fitted line was 0.017 ± 0.006 and the intercept was $(5.7 \pm 1.8) \times 10^4$ Pa. A positive intercept of ≅8 psi suggests a baseline pressure drop associated with the viscous flow of water through the pores. A variation in the pore characteristics with plate thickness, notably, a higher porosity near the surface than in the interior, could also be a reason for this additional pressure drop.

The R^2 for the linear correlation between ΔP_g and ξ was significantly higher ($R^2 \cong 0.96$) than that for the linear correlation between ΔP_g and $\gamma/\sqrt{K/\varepsilon}$, which does not account for the differences in the surface wettability of the pores. For the latter correlation, R^2 was only ≅0.43. The correlation between ΔP_g and ξ was stronger than that between ΔP_g and ε ($R^2 = 0.69$). A linear correlation between P_c and K was not statistically significant.

According to the capillary bundle model, the slope, J, of the capillary pressure versus ξ is related to tortuosity, τ, by

$$J = \frac{1}{\sqrt{2\tau}} \tag{17}$$

The experimentally determined $J = 0.017$ yields a relatively high tortuosity of about 1780. The high tortuosity is expected based on the complex shape and interconnectedness of the pores in the graphite composite (Figure 3d). Furthermore, the

https://doi.org/10.1021/acs.iecr.1c01737
Ind. Eng. Chem. Res. XXXX, XXX, XXX−XXX

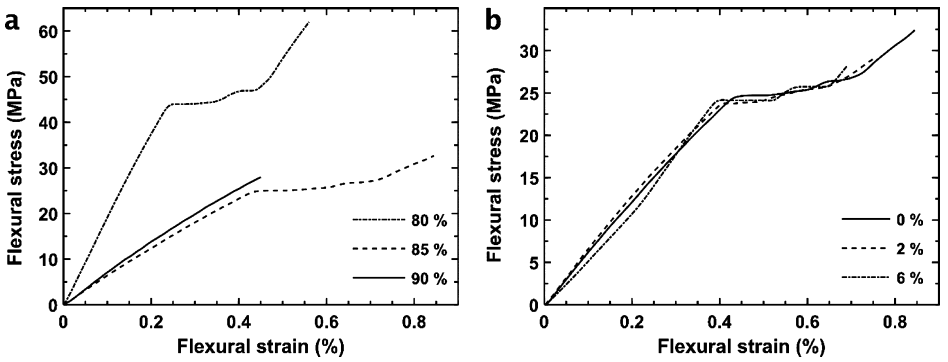

Figure 12. Representative stress vs strain plots from the flexural testing of graphite plates prepared using (a) different concentrations of graphite without porogen and (b) 85 wt % graphite and different concentrations of sucrose porogen.

Table 2. Effect of Graphite and Porogen Concentration on the Mechanical Properties of the Graphite−Resol Composite Plates

sample	graphite (wt %)	polymer (wt %)	porogen (%)	flexural modulus (GPa)	yield strength (MPa)	flexural strength (MPa)
80G-0P	80	20	0	20(2)[a]	41(4)	61(2)
85G-0P	85	15	0	6.4(4)[a]	25(2)	34(2)
90G-0P	90	10	0	6.4(4)	25(2)	26(3)
85G-2P, 85G-6P	85	15	2, 6	6.1(7)	23(2)	29(3)

[a]The number enclosed in parenthesis gives the uncertainty in the least significant digit of the reported value; 20(2) means 20 ± 2 and 6.4(4) means 6.4 ± 0.4.

equivalent pore radius, r, based on the tube bundle model is related to J as

$$r = \frac{2}{J}\sqrt{\frac{K}{\varepsilon}} \tag{18}$$

The tube radius was found to be in the range of 1.2 ± 0.2 μm for all the plates prepared using 10% sucrose porogen.

3.6. Electrical Conductivity. Figure 11 shows the electrical conductivity of the various graphite plates investigated in the present study. The through-plane conductivity was determined using eq 1, from the variation of the voltage drop across the thickness of the plate for different current densities (see Figure S9 in Supporting Information). All the plates exhibited a conductivity higher than 100 S cm^{-1}, significantly greater than the through-plane conductivities of some graphite−polymer composite plates previously reported in the literature.[21,22,27] The higher through-plane conductivity is attributed to the use of high-aspect-ratio graphite particles (cf. Figure 3b), the lower compression molding pressure (9.58 bar compared with 68.9 bar used by Huang et al.[22]) leading to a more random orientation and better interparticle contact of the conductive graphite flakes, and the higher graphite concentration in the plates of the present study (80−90 wt % compared with 64−70 wt % used in other graphite−polymer composites[21]). The conductivity increased with an increase in the graphite concentration (Figure 11a) and decreased with an increase in the porogen concentration (Figure 11b). In both cases, a higher volume of the conductive graphite particles, relative to the non-conductive polymer resin in the former and pores in the latter, resulted in higher electrical conductivity. The conductivity was about 240 S cm^{-1} for the plate prepared without using a porogen and 140 S cm^{-1} for the plate prepared using 10% of the sucrose porogen. The porosities of these plates were about 18 and 41%, respectively. The conductivity did not show a significant difference when the plate prepared using 10% of the porogen was further treated with aqueous H_2O_2 and H_2SO_4 + H_2O_2 solutions. However, the plate treated by heating at 400 °C in air showed a lower conductivity of 112 S cm^{-1}, which is attributed to its higher porosity (≅49%).

3.7. Mechanical Properties. Figure 12 shows the results of the flexural testing of the graphite plates at room temperature. The flexural stress, σ_f, was calculated using the simple-beam formula

$$\sigma_f = \frac{3FL}{2wt^2} \tag{19}$$

where F is the applied load, L is the distance between the support points (≅25.4 mm), t is the thickness of the plate along the direction of the applied load (≅1.5 mm), and w is the specimen width. The flexural strain, ε_f, of an element of the outer surface of the test specimen at the midspan was calculated using

$$\varepsilon_f = \frac{6\delta t}{L^2} \tag{20}$$

where δ is the maximum deflection of the center of the specimen.

The flexural modulus is the slope of the linear region of the stress versus strain plot before the yield point. The yield strength is defined as the lowest stress at which the stress versus strain plot shows a sharp change in the slope (and the onset of significant nonlinearity). The flexural strength, σ_{fs}, was calculated to be $3F_{fs}L/(2wt^2)$, where F_{fs} is the load at the fracture.

Figure 12a shows the effect of the graphite concentration, and Figure 12b shows the impact of the porogen concentration on the stress versus strain behavior of the porous plates. The mechanical properties of graphite plates were highly sensitive to the graphite concentration (conversely, the polymer concentration in the plate), especially in the range of 80−85 wt % of graphite (20−15 wt % of the phenolic resin). The flexural modulus, yield strength, and flexural strength values were significantly higher for the plate containing 20 wt % of the polymer binder than the plates with 15 or 10 wt % of the

https://doi.org/10.1021/acs.iecr.1c01737
Ind. Eng. Chem. Res. XXXX, XXX, XXX−XXX

polymer (see Table 2). In contrast, in the range of 0−6%, the porogen concentration did not have a significant effect on the flexural modulus and yield strength of the plates, but the flexural strength showed a slight decrease with an increase in the porogen concentration and porosity of the plates.

The flexural strength, σ_{fs}, of the plate prepared without using the porogen was 34 ± 2 MPa, which was statistically higher ($p < 0.05$) than the plates prepared using the porogen. The σ_{fs} of the plates prepared using 2 and 6% porogens were not statistically different from each other and ≅29 ± 3 MPa. The σ_{fs} of the plates prepared using 10% porogen and surface treated with aqueous solutions of H_2O_2 and H_2SO_4 + H_2O_2 were also not significantly different from each other (or from that of the untreated plates) and was equal to 28 ± 4 MPa. However, there was a significant decrease in σ_{fs} of the plates treated by air oxidation at 400 °C, during which more of the organic resin is removed from the plate by thermal degradation. The σ_{fs} of these thermally treated plates were 19 ± 2 MPa, the lowest in the set. These results indicate that the flexural strength of the porous graphite plates is primarily dependent on the presence of the phenolic resin in the composite plates (see the values for 80G-0P, 85G-0P, and 90G-0P in Table 2) and less so on the porosity of the plates (compare the values for 85G-0P, 85G-2P, 85G-6P, and 85G-10P with porosities of ≅19, 23, 33, and 41% respectively). Nevertheless, the partial removal of the resin from 85G-10P by thermal degradation resulted in an increase in the porosity to about 49% and decreased the flexural strength by about 30%.

3.8. Optimal Surface Treatment Method. Thermal oxidation 85G-10P in air resulted in the highest permeability of 57 μD compared with oxidation using aqueous H_2SO_4 + H_2O_2 and H_2O_2 (≅56 and 46 μD, respectively). The water contact angle was the lowest for the thermally treated plates (Figure 8). Consequently, the capillary pressure, and the gas-breakthrough pressure, was the highest for the thermally treated plates. ΔP_g was ≅20 psi for the heat-treated plate, 15 psi for the H_2O_2-treated plates, 13 psi for the H_2SO_4 + H_2O_2-treated plates. The electrical conductivity of the thermally treated plate was lower (≅112 S cm^{-1}) than the H_2SO_4 + H_2O_2- or the H_2O_2-treated plates (≅133 and 121 S cm^{-1}, respectively). The flexural strength of the thermally treated plate was also lower (≅19 MPa) than the H_2SO_4 + H_2O_2- and H_2O_2-treated plates (≅28 MPa). Based on these results, the H_2SO_4 + H_2O_2-treated plates are found to have an optimal combination of water permeability, gas-breakthrough pressure, electrical conductivity, and flexural strength.

4. CONCLUSIONS

A method of preparing porous, electrically conductive graphite plates of good flexural strength was developed using a sacrificial porogen and a compression molding process at lower-processing temperatures than previous reports.[29] Using sucrose as the sacrificial porogen, we obtained plates with controlled porosity and permeability, which is difficult to achieve using other methods such as pyrolytic pore formation. The porosity varied linearly with the concentration of the porogen in the composite mixture. Water permeability through the plates could be increased by the chemical or thermal oxidation of the surfaces of the pores to increase their hydrophilicity. A measurable increase in permeability was observed by relatively simple treatments such as immersing the porous plates in aqueous hydrogen peroxide and sulfuric acid solutions for 30 min at room temperature.

The high electrical conductivity observed for the graphite plates was because of the relatively high amount of conductive graphite in the composite (in the range of 80−90 wt %) compared with the non-conductive phenolic resin binder. The phenolic resin was an important factor in determining the flexural strength of the porous graphite plates. A relatively small amount of the resin (≅15 wt %) was found sufficient to obtain good flexural strength. However, the oxidation of the polymer, and a decrease in its concentration by thermal degradation and volatilization at 400 °C, caused a noticeable reduction in the flexural strength of the composite.

In applications such as bipolar plates for PEM fuel cells, the porous plate must block gas leakage through them. Contrary to the possibility that a more porous plate would be more gas-permeable, the gas blocking ability of the porous plates of the present study increased with an increase in the porosity of the plates. The increase in the gas-breakthrough pressure is attributed to the capillary pressure at the gas−liquid interface of the water-filled micropores, which opposes the gas flow through the porous channels. The gas-breakthrough pressure was found to be linearly correlated with the capillary pressure.

The porous graphite plates, prepared using 10% of sucrose porogens and chemically treated to impart surface hydrophilicity, exhibited electrical conductivity and flexural strength that exceeded the U.S. Department of Energy (DOE) targets of 100 S cm^{-1} and 25 MPa, respectively, for bipolar plates for transportation applications.[50] These plates also exhibited a significant water uptake and permeability that would enable efficient water management in the fuel cell. A further improvement in the water transport properties would be possible with an increase in the plate's porosity through the increased porogen concentration. Though the electrical conductivity does not decrease much with an increase in the porogen concentration beyond 10% (cf. Figure 11b), any further increase in the porosity would decrease the flexural strength below the target of 25 MPa. Incorporating high-aspect-ratio conductive filler particles, such as carbon fibers, along with the graphite flakes could be explored to increase the flexural strength, while further increasing the rate of water uptake by the porous bipolar plates. Considering the relatively simple production and the good liquid and gas transport properties, electrical conductivity, and mechanical properties, the porous graphite composite of the reported study seems promising for addressing the water management issues in fuel cells.

■ ASSOCIATED CONTENT

Supporting Information

The Supporting Information is available free of charge at https://pubs.acs.org/doi/10.1021/acs.iecr.1c01737.

Attenuated total reflectance FTIR spectroscopy, thermogravimetry, and differential scanning calorimetry analysis of the phenolic resin, determination of surface roughness of the graphite plate using optical interferometry and triangulation, and measurement of its through-plane electrical conductivity using voltage versus current density data (PDF)

■ AUTHOR INFORMATION

Corresponding Author

Sitaraman Krishnan − *Department of Chemical and Biomolecular Engineering, Clarkson University, Potsdam,*

https://doi.org/10.1021/acs.iecr.1c01737
Ind. Eng. Chem. Res. XXXX, XXX, XXX−XXX

New York 13699, United States; orcid.org/0000-0002-1228-8393; Phone: +1 315 268 6661; Email: skrishna@clarkson.edu

Authors

Aswin Prathap Pitchiya − *Department of Chemical and Biomolecular Engineering, Clarkson University, Potsdam, New York 13699, United States*

Ngoc-Tram Le − *Department of Chemical and Biomolecular Engineering, Clarkson University, Potsdam, New York 13699, United States;* orcid.org/0000-0002-7490-1835

Zackary A. Putnam − *Department of Chemical and Biomolecular Engineering, Clarkson University, Potsdam, New York 13699, United States; Materials Science and Engineering Ph.D. Program, Clarkson University, Potsdam, New York 13699, United States*

Michael Harrington − *US Hybrid Corporation, South Windsor, Connecticut 06074, United States*

Complete contact information is available at: https://pubs.acs.org/10.1021/acs.iecr.1c01737

Notes

The authors declare no competing financial interest.

■ ACKNOWLEDGMENTS

The research was funded by US Hybrid Corporation. The use of experimental facilities supported by the Center for Advanced Materials Processing, a New York State Center for Advanced Technology, at Clarkson University, is gratefully acknowledged. XPS data were acquired at the Cornell Center for Materials Research Shared Facilities, which are supported through the NSF MRSEC program (DMR-1719875).

■ LIST OF SYMBOLS

A	cross-sectional area of the flow through the plate (m^2)
E_v	vacuum-fill mass gain (%)
E_w	wick-fill mass gain (%)
F	applied load (N)
F_{fs}	load at fracture (N)
J	Leverett *J*-function
K	permeability (m^2)
l	plate length (m)
L	distance between support points in flexural testing (m)
m_1	dry mass of the plate (kg)
m_{2a}	mass of wick-filled plate (kg)
m_{2v}	mass of vacuum-filled plate (kg)
m_3	mass of vacuum-filled plate suspended in water (kg)
P_c	capillary pressure (Pa)
ΔP	pressure difference in permeability measurement (Pa)
ΔP_g	gas-breakthrough pressure (Pa)
r	pore radius in the tube bundle model (m)
R	plate resistance (ohm)
R_1	resistance of the plate/carbon-cloth assembly (ohm)
R_2	resistance of the carbon cloth (ohm)
t	plate thickness (m)
V	total plate volume (m^3)
V_i	volume of impervious portion (m^3)
V_o	volume of open pores (m^3)
v	normalized specific volume ($m^3\ kg^{-1}$)
v_i	normalized impervious volume ($m^3\ kg^{-1}$)
v_o	normalized open pore volume ($m^3\ kg^{-1}$)
Q	volumetric flow rate ($m^3\ s^{-1}$)
w	plate width (m)
γ	surface energy ($J\ m^{-2}$) or surface tension ($N\ m^{-1}$)
γ_s^d	dispersion component of the surface energy ($J\ m^{-2}$)
δ	maximum deflection in flexural testing (m)
ε	porosity (%)
ε_f	flexural strain (%)
η	viscosity (Pa s)
θ	contact angle (°)
$\overline{\theta}$	average contact angle (°)
θ_a	advancing contact angle (°)
θ_r	receding contact angle (°)
θ_w	water contact angle (°)
κ	conductivity ($S\ m^{-1}$)
ξ	capillary pressure factor (Pa)
ρ_w	density of water ($kg\ m^{-3}$)
σ_f	flexural stress (Pa)
σ_{fs}	flexural strength (Pa)
τ	tortuosity

■ REFERENCES

(1) Wang, X. R.; Ma, Y.; Gao, J.; Li, T.; Jiang, G. Z.; Sun, Z. Y. Review on water management methods for proton exchange membrane fuel cells. *Int. J. Hydrogen Energy* **2021**, *46*, 12206−12229.

(2) Kandlikar, S. G. Microscale and macroscale aspects of water management challenges in PEM fuel cells. *Heat Transfer Eng.* **2008**, *29*, 575−587.

(3) Vincent, I.; Lee, E.-C.; Kim, H.-M. Solutions to the water flooding problem for unitized regenerative fuel cells: status and perspectives. *RSC Adv.* **2020**, *10*, 16844−16860.

(4) Lebga-Nebane, J. L.; Rock, S. E.; Franclemont, J.; Roy, D.; Krishnan, S. Thermophysical properties and proton transport mechanisms of trialkylammonium and 1-alkyl-1*H*-imidazol-3-ium protic ionic liquids. *Ind. Eng. Chem. Res.* **2012**, *51*, 14084−14098.

(5) Steinbach, A. J.; Allen, J. S.; Borup, R. L.; Hussey, D. S.; Jacobson, D. L.; Komlev, A.; Kwong, A.; MacDonald, J.; Mukundan, R.; Pejsa, M. J.; Roos, M.; Santamaria, A. D.; Sieracki, J. M.; Spernjak, D.; Zenyuk, I. V.; Weber, A. Z. Anode-design strategies for improved performance of polymer-electrolyte fuel cells with ultra-thin electrodes. *Joule* **2018**, *2*, 1297−1312.

(6) Park, Y.; Caton, J. An experimental investigation of electro-osmotic drag coefficients in a polymer electrolyte membrane fuel cell. *Int. J. Hydrogen Energy* **2008**, *33*, 7513−7520.

(7) Taniguchi, A.; Yasuda, K. Highly water-proof coating of gas flow channels by plasma polymerization for PEM fuel cells. *J. Power Sources* **2005**, *141*, 8−12.

(8) Owejan, J.; Trabold, T.; Jacobson, D.; Arif, M.; Kandlikar, S. Effects of flow field and diffusion layer properties on water accumulation in a PEM fuel cell. *Int. J. Hydrogen Energy* **2007**, *32*, 4489−4502.

(9) Tang, H.-Y.; Santamaria, A.; Park, J. W.; Lee, C.; Hwang, W. Quantification of water in hydrophobic and hydrophilic flow channels subjected to gas purging via neutron imaging. *J. Power Sources* **2011**, *196*, 9373−9381.

(10) Jung, G.-B.; Sun, L.-M.; Jao, T.-C.; Hunag, B.-W.; Liu, Y.-H. Hydrophobic PTFE-coated serpentine flow fields with ladder-structure for fuel cell application. *Int. J. Hydrogen Energy* **2012**, *37*, 15820−15826.

(11) Schade, M.; Franzka, S.; Cappuccio, F.; Peinecke, V.; Heinzel, A.; Hartmann, N. Photothermally induced bromination of carbon/polymer bipolar plate materials for fuel cell applications. *Appl. Surf. Sci.* **2015**, *336*, 85−88.

(12) Ge, S.-H.; Li, X.-G.; Hsing, I.-M. Water management in PEMFCs using absorbent wicks. *J. Electrochem. Soc.* **2004**, *151*, B523−B528.

(13) Simon, C.; Endres, J.; Nefzger-Loders, B.; Wilhelm, F.; Gasteiger, H. A. Interaction of pore size and hydrophobicity/hydrophilicity for improved oxygen and water transport through microporous layers. *J. Electrochem. Soc.* **2019**, *166*, F1022−F1035.

(14) Simon, C.; Kartouzian, D.; Müller, D.; Wilhelm, F.; Gasteiger, H. A. Impact of microporous layer pore properties on liquid water transport in PEM fuel cells: carbon black type and perforation. *J. Electrochem. Soc.* **2017**, *164*, F1697−F1711.
(15) Forner-Cuenca, A.; Biesdorf, J.; Lamibrac, A.; Manzi-Orezzoli, V.; Büchi, F. N.; Gubler, L.; Schmidt, T. J.; Boillat, P. Advanced water management in PEFCs: Diffusion layers with patterned wettability III. Operando characterization with neutron imaging. *J. Electrochem. Soc.* **2016**, *163*, F1038−F1048.
(16) Spernjak, D.; Mukundan, R.; Borup, R. L.; Connolly, L.; Zackin, B.; De Andrade, V.; Wojcik, M.; Parkinson, D. Y.; Jacobson, D.; Hussey, D. S. Enhanced water management of polymer electrolyte fuel cells with additive-containing microporous layers. *ACS Appl. Energy Mater.* **2018**, *1*, 6006−6017.
(17) Xiong, Z. a.; Liao, S.; Dang, D.; Tian, X.; Hou, S.; Liu, F.; Peng, H.; Fu, Z. Enhanced water management in the cathode of an air-breathing PEMFC using a dual catalyst layer and optimizing the gas diffusion and microporous layers. *Int. J. Hydrogen Energy* **2015**, *40*, 3961−3967.
(18) Shi, J.; Zhang, P.; Han, Y.; Wang, H.; Wang, X.; Yu, Y.; Sun, J. Investigation on electrochemical behavior and surface conductivity of titanium carbide modified Ti bipolar plate of PEMFC. *Int. J. Hydrogen Energy* **2020**, *45*, 10050−10058.
(19) Wu, Y.; Cho, J. I. S.; Whiteley, M.; Rasha, L.; Neville, T. P.; Ziesche, R.; Xu, R.; Owen, R.; Kulkarni, N.; Hack, J.; Maier, M.; Kardjilov, N.; Markötter, H.; Manke, I.; Wang, F. R.; Shearing, P. R.; Brett, D. J. L. Characterization of water management in metal foam flow-field based polymer electrolyte fuel cells using in-operando neutron radiography. *Int. J. Hydrogen Energy* **2020**, *45*, 2195−2205.
(20) Madadi, F.; Rezaeian, A.; Edris, H.; Zhiani, M. Influence of surface roughness and hydrophobicity of bipolar plates on PEM performance. *Surf. Coat. Technol.* **2020**, *389*, 125676.
(21) Cunningham, B.; Baird, D. G. The development of economical bipolar plates for fuel cells. *J. Mater. Chem.* **2006**, *16*, 4385−4388.
(22) Huang, J.; Baird, D. G.; McGrath, J. E. Development of fuel cell bipolar plates from graphite filled wet-lay thermoplastic composite materials. *J. Power Sources* **2005**, *150*, 110−119.
(23) Yao, K.; Adams, D.; Hao, A.; Zheng, J. P.; Liang, Z.; Nguyen, N. Highly conductive and strong graphite-phenolic resin composite for bipolar plate applications. *Energy Fuels* **2017**, *31*, 14320−14331.
(24) Soleimani Alavijeh, M.; Kefayati, H.; Nozad Golikand, A.; Shariati, S. Synthesis and characterization of epoxy/graphite/nano-copper nanocomposite for the fabrication of bipolar plate for PEMFCs. *J. Nanostruct. Chem.* **2019**, *9*, 11−18.
(25) Kuan, Y.-D.; Ciou, C.-W.; Shen, M.-Y.; Wang, C.-K.; Fitriani, R. Z.; Lee, C.-Y. Bipolar plate design and fabrication using graphite reinforced composite laminate for proton exchange membrane fuel cells. *Int. J. Hydrogen Energy* **2021**, *46*, 16801−16814.
(26) Kahveci, E. E.; Taymaz, I. Experimental study on performance evaluation of PEM fuel cell by coating bipolar plate with materials having different contact angle. *Fuel* **2019**, *253*, 1274−1281.
(27) Alo, O. A.; Otunniyi, I. O.; Pienaar, H. Development of graphite-filled polymer blends for application in bipolar plates. *Polym. Compos.* **2020**, *41*, 3364−3375.
(28) Zhang, G.; Kandlikar, S. G. A critical review of cooling techniques in proton exchange membrane fuel cell stacks. *Int. J. Hydrogen Energy* **2012**, *37*, 2412−2429.
(29) Gorman, M. E. Method of using a water transport plate. U.S. Patent 6,197,442 B1, 2001.
(30) ASTM International. *Standard test methods for flexural properties of unreinforced and reinforced plastics and electrical insulating materials*; ASTM D790-17; West Conshohocken, PA, 2017. https://www.astm.org/Standards/D790.htm.
(31) Pilato, L. Phenolic resins: 100 Years and still going strong. *React. Funct. Polym.* **2013**, *73*, 270−277.
(32) Conner, A. H. Wood: Adhesives. In *Encyclopedia of Materials: Science and Technology*; Buschow, K. H. J., Cahn, R. W., Flemings, M. C., Ilschner, B., Kramer, E. J., Mahajan, S., Veyssière, P., Eds.; Elsevier: Oxford, 2001; pp 9583−9599.
(33) Krishnan, S.; Klein, A.; El-Aasser, M. S.; Sudol, E. D. Influence of chain transfer agent on the cross-linking of poly(*n*-butyl methacrylate-*co*-*N*-methylol acrylamide) latex particles and films. *Macromolecules* **2003**, *36*, 3511−3518.
(34) Rattanaumpa, T.; Naowanon, W.; Amnuaypanich, S.; Amnuaypanich, S. Polydimethylsiloxane sponges incorporated with mesoporous silica nanoparticles (PDMS/H-MSNs) and their selective solvent absorptions. *Ind. Eng. Chem. Res.* **2019**, *58*, 21142−21154.
(35) British Standards Institution. *Ceramic tiles—Part 3: Determination of water absorption, apparent porosity, apparent relative density and bulk density*; BS EN ISO 10545-3:2018, 2018. https://www.iso.org/standard/68006.html.
(36) Gupta, R.; Maloney, D. R. Intercept method−A novel technique to correct steady-state relative permeability data for capillary end effects. *SPE Reservoir Eval. Eng.* **2016**, *19*, 316−330.
(37) Prydatko, A. V.; Belyaeva, L. A.; Jiang, L.; Lima, L. M. C.; Schneider, G. F. Contact angle measurement of free-standing square-millimeter single-layer graphene. *Nat. Commun.* **2018**, *9*, 4185.
(38) Ondarçuhu, T.; Thomas, V.; Nuñez, M.; Dujardin, E.; Rahman, A.; Black, C. T.; Checco, A. Wettability of partially suspended graphene. *Sci. Rep.* **2016**, *6*, 24237.
(39) Aria, A. I.; Kidambi, P. R.; Weatherup, R. S.; Xiao, L.; Williams, J. A.; Hofmann, S. Time evolution of the wettability of supported graphene under ambient air exposure. *J. Phys. Chem. C* **2016**, *120*, 2215−2224.
(40) Raj, R.; Maroo, S. C.; Wang, E. N. Wettability of graphene. *Nano Lett.* **2013**, *13*, 1509−1515.
(41) Shin, Y. J.; Wang, Y.; Huang, H.; Kalon, G.; Wee, A. T. S.; Shen, Z.; Bhatia, C. S.; Yang, H. Surface-energy engineering of graphene. *Langmuir* **2010**, *26*, 3798−3802.
(42) Fowkes, F. M.; Harkins, W. D. The state of monolayers adsorbed at the interface solid-aqueous solution. *J. Am. Chem. Soc.* **1940**, *62*, 3377−3386.
(43) Fowkes, F. M. Dispersion force contributions to surface and interfacial tensions, contact angles, and heats of immersion. In *Contact Angle, Wettability, and Adhesion*; Americal Chemical Society, 1964; Vol. *43*, pp 99−111.
(44) Morcos, I. On contact angle and dispersion energy of the cleavage graphite/water system. *J. Colloid Interface Sci.* **1970**, *34*, 469−471.
(45) Kang, W.; Li, H. Enhancement of flaky graphite cleaning by ultrasonic treatment. *R. Soc. Open Sci.* **2019**, *6*, 191160.
(46) Wang, S.; Zhang, Y.; Abidi, N.; Cabrales, L. Wettability and surface free energy of graphene films. *Langmuir* **2009**, *25*, 11078−11081.
(47) Possart, W.; Kamusewitz, H. Wetting and scanning force microscopy on rough polymer surfaces: Wenzel's roughness factor and the thermodynamic contact angle. *Appl. Phys. A: Mater. Sci. Process.* **2003**, *76*, 899−902.
(48) Leverett, M. C. Capillary behavior in porous solids. *Trans. AIME* **1941**, *142*, 152−169.
(49) Xu, W. S.; Luo, P. Y.; Sun, L.; Lin, N. A prediction model of the capillary pressure *J*-function. *PLoS One* **2016**, *11*, No. e0162123.
(50) Kopasz, J. P.; Benjamin, T. G.; Schenk, D. *Bipolar Plate Workshop Summary Report*; U. S. Department of Energy and Argonne National Laboratory, 2017. https://publications.anl.gov/anlpubs/2017/11/137641.pdf.

https://doi.org/10.1021/acs.iecr.1c01737
Ind. Eng. Chem. Res. XXXX, XXX, XXX−XXX